Applied Thermal Engineering 169 (2020) 114932

Contents lists available at ScienceDirect

Applied Thermal Engineering

journal homepage: www.elsevier.com/locate/apthermeng

Optimization of the automotive air conditioning strategy based on the study of dewing phenomenon and defogging progress

Yue Yang[a,b], Yuqi Huang[a,*], Jisheng Zhao[c]

[a] Department of Energy Engineering, Zhejiang University, Hangzhou 310027, China
[b] Department of Computer and Information Science, University of Pennsylvania, Philadelphia, PA 19104, USA
[c] Fluids Laboratory for Aeronautical and Industrial Research, Department of Mechanical and Aerospace Engineering, Monash University, Clayton, VIC 3800, Australia

HIGHLIGHTS

- Numerically studied the dewing and defogging progress of a truck cabin;
- The external flow field was analyzed to get convective heat transfer coefficient;
- Effect of air velocity, temperature and humidity was considered and compared;
- Optimal control strategy of air conditioner was concluded based on these studies.

ARTICLE INFO

Keywords:
Vehicular window dewing
Phase change
Condensation
Defog
Air conditioning

ABSTRACT

The problem of vehicle window dewing not only affects the occupants' comfort, but also interferes with the driver's sight and potentially threatens the safety of driving as well as electronic equipment in the vehicle. Therefore, analyzing the condensation process inside the cabin is of great practical concern to improve driving comfort and safety. This study focuses on the process of condensation and defogging in the cabin of a truck model, where the outside heat dissipation and internal air conditioning system are considered together. The condensation process simulation based on the EWF (Eulerian Wall Film) model in conjunction with user defined functions was validated by comparing with experiments. Then, the flow domain around a simplified three-dimensional truck model was established to conduct the external thermal conditions. By examining various conditions of the air inlet mode, temperature, humidity and speeds of the ventilation system, it was found that the mass flow rate, inlet temperature and humidity could influence the dewing film thickness directly. Of significance, when the air conditioning system was taken as the main defogging approach, with the relative humidity set at approximately 20% and the temperature above 320 K, the dewing phenomenon was eliminated at the highest efficiency. This paper also found that the comfortable, efficiency and safety requirements could all be obtained when the relative humidity was within the range of 20% $<$ RH $<$ 60% and the temperature range of 292 K $<$ T $<$ 298 K. These results would be useful to provide suggestions for the future design of automotive air conditioning systems.

1. Introduction

Dewing is a very common phenomenon, as it refers to vapor condensing on the surface of an object when the temperature is lower than a critical (dewing) point. In engineering applications, it can potentially cause severe hazards. For example, dewing in pipes and equipment will accelerate corrosion process and reduce the component life; bacteria in human nasal cavity can reproduce rapidly in dews, causing respiratory diseases [1]. Similar to human beings, vehicles are also severely affected by dewing problem in the cabin. Dews on the vehicle windows would not only influence the sight of the driver, potentially leading to a traffic accident, but also increase the humidity inside the vehicle, affecting the comfort of occupants. With the increasing number and complexity of electronic devices in vehicles, which are sensitive to the humidity and temperature, the vehicular control system can also be affected by dewing problem.

To deal with the dewing problem, three primary methods have often been discussed: changing the ventilation condition, raising the window

* Corresponding author.
E-mail address: huangyuqi@zju.edu.cn (Y. Huang).

https://doi.org/10.1016/j.applthermaleng.2020.114932
Received 30 September 2019; Received in revised form 10 December 2019; Accepted 9 January 2020
Available online 16 January 2020
1359-4311/

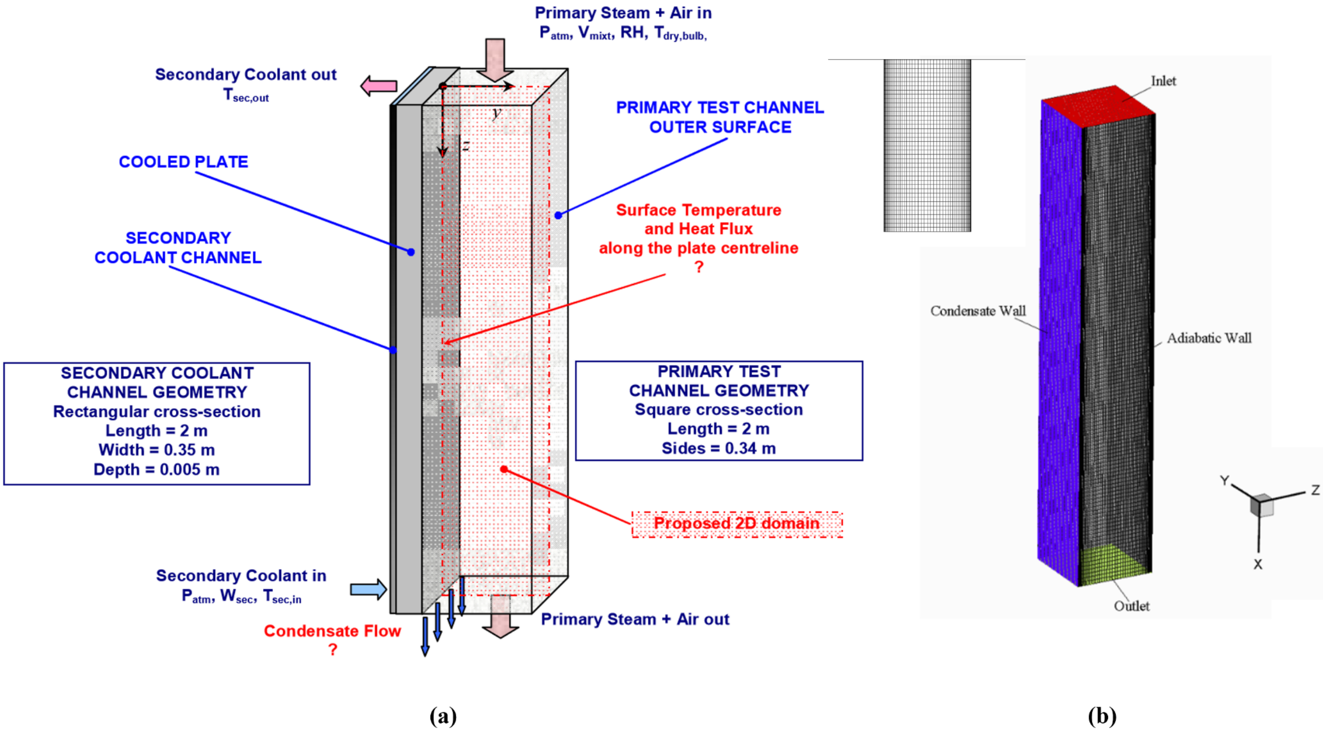

Fig. 1. Schematics of (a) the experimental model used by Ambrosini [35] and (b) the finite element model and its near-wall grids. Note that the wet air flow moves from the top to the bottom through a square cross-sectional pipe, and it condenses on the cooled surfaces.

Table 1
Inlet Parameters of Validation Model.

Cases	Inlet Parameters			
	V[m/s]	RH[%]	T[°C]	ω_{vap}
P30-T40-V25	2.63	100	97.5	0.8692
P20-T40-V25	2.59	100	89.5	0.5685
P10-T40-V25	2.58	100	79.8	0.3500

P - pressure; T - temperature; V - velocity; ω_{vap}- the mass fraction of water vapor.

surface temperature, and using anti-fogging materials. However, the latter two have considerable drawbacks; for example, the technique of adding the heating wire in the glass to raise window surface temperature may not be applicable in the front window for the reason of blocking eyesight. Anti-fogging materials, such as anti-clouding agent and soapy water, could reduce the surface tension of water to promote membrane condensation, but the effective time duration of this approach is very short, and it may emit peculiar smell and harmful gases (VOC). Thus, controlling the air conditioning system appears to be the most widely used method of defogging, despite energy consumption. Therefore, it is of significant interest to investigate various operating conditions of a ventilating system to efficiently diminish the dew phenomenon.

Condensation is a kind of complicated two-phase flow which occurs frequently in various industrial facilities and engineering systems and has attracted considerable attention. The process of phase change of the flow can be strongly affected by its thermal status, while condensation on surface, in turn, will have influence on the heat transfer performance. Li et al. [2] conducted the simulation and experimental on the condensation of a staggered tube bundle heat exchanger, showing that the CFD model could predict the temperature and condensate mass rate very well. Serrano et al. [3] established an in-flow water condensation model, and successfully simulated the bulk flow condensation caused by the mixing of air streams in a long route EGR system. Yi et al. [4] carried a visualized experiment to observe the water vapor condensation on an isothermal vertical industrial common aluminum plate. Ghafari et al. [5] even developed a new turbulence model to simulate the direct contact condensation in a two-phase flow with thermal shock. While a large amount of work on dewing phenomenon has been focused on buildings [6,7], nuclear services [8,9], heat transfer pipe systems [10–12], much less research attention has been paid to the dewing problem of vehicle windows. Previous studies have shown that CFD (Computational Fluid Dynamics) method is a validated approach for analyzing the airflow conditions and water vapor condensation progress in various circumstances [13–15]. At the end of last century, Hara and Fujitani [16] conducted a series of two- and three-dimensional (2-D and 3-D) simulations on the airflow and temperature field inside a car cabin, showing that numerical simulations could perfectly reflect the heat transfer and flow process. You et al. [17] simulated the moisture condensation of a chamber model to predict its inner hygrothermal distribution in a high humidity climate and established two regression equations to describe relationships between the indoor air temperature, humidity and parametric factors of the infiltrated air. Through numerical simulations, Somnath and Mayur [18] analyzed the thermal comfort and airflow distribution inside a vehicle cabin and reported that the flow field on passengers as well as inside the cabin strongly affected the overall cooling rate. Saboora and Kim [19] numerically analyzed the thermal and flow field in a vehicle cabin to predict the human thermal comfort and energy consumption under different ventilation conditions. Some other studies have also been dedicated to solving the contest of thermal comfort and energy consumption. Myoung Su Oh et al. [20] investigated both thermal comfort in the vehicle compartment and energy saving of the localized air-conditioning system with front and ceiling vents. Schaut and Sawodny [21] used an optimization-based approach to minimize the energy consumption of thermal system while maximizing the thermal comfort of occupants for battery electric vehicle models. Zhang et al. [22] established a comprehensive model to evaluate the total annual energy consumption of an electric vehicle air conditioning system in different cities across China, where the cabin thermal comfort and climate

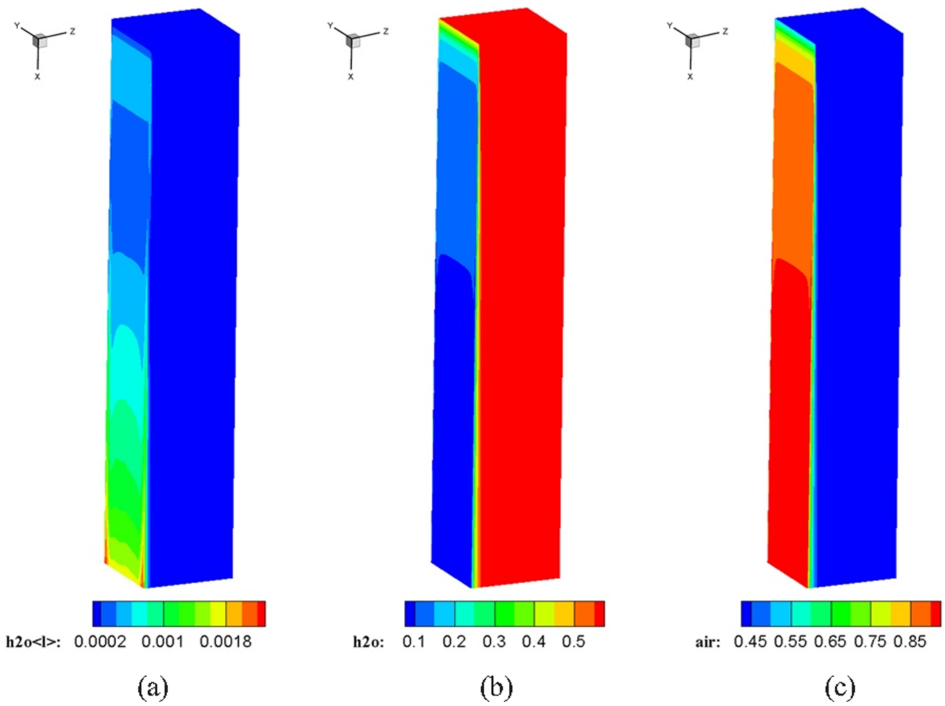

Fig. 2. Distribution of the mass fraction (a) liquid water, (b) gaseous water and (c) air.

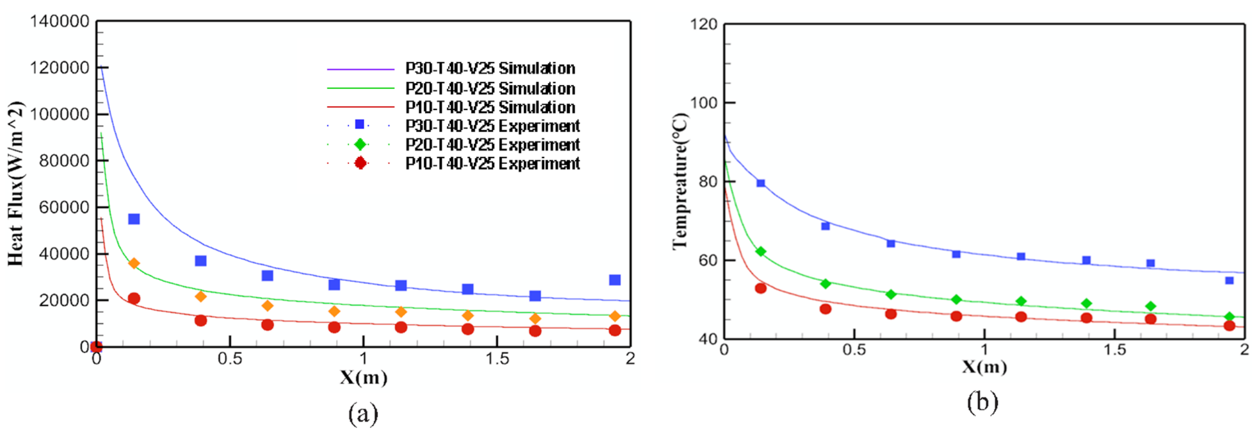

Fig. 3. (a) Comparisons of the heat flux along the wall in the X-direction between the present numerical results and the previous experimental measurements by Ambrosini [35] (b) Comparisons of the temperature along the wall in the X-direction between present numerical results and the previous experimental measurements by Ambrosini [35].

control load approach were taken as the basic factors. Zhang et al. [23] conducted numerical simulations for the inside of a vehicle model, suggesting that for the thermal comfort the compartment temperature should be with the range of 24–29 °C and the local velocity should not be larger than 0.5 m/s. Andreea et al. [24] suggested that relatively humidity between 30% and 70% did not have an influence on the thermal comfort at neutral temperatures.

Most of previous studies on the thermal comfort of vehicular cabin have focused on the thermal status and flow fields, but only a few of them have considered the dewing process of window glass and its negative effects. Taro Ono et al. [25] noticed the contradiction between defogging and energy saving performance. They performed an unsteady simulation to evaluate both the defogging performance and thermal comfort, and to analyze the corresponding air-conditioning load to find an optimized control strategy. Abdulnour et al. [26,27] and Aroussi et al. [28–30] conducted both experiments and numerical simulations to investigate the defrosting and demisting performance, but with little attention given to the dewing process. Dwiartono [31] numerically investigated the defogging characteristics of vehicle windows. In their numerical simulations, the fog layer attached to the glass surface was considered as a liquid film of the same thickness, and two models were used: on model for analyzing one-dimensional unsteady heat transfer, and the other for simulating the evaporation characteristics of the liquid film. Kharat and Nandgaokar [32] also simulated the internal heat environment of a vehicle model and analyzed the mechanism of fogging and defogging on the window surfaces. However, these studies were mainly focused on the phase transform on the front windshield, neglecting the side and rear windows, where the distribution of humidity and temperature field in the cabin was not considered, and also the influence of external flow fields was ignored.

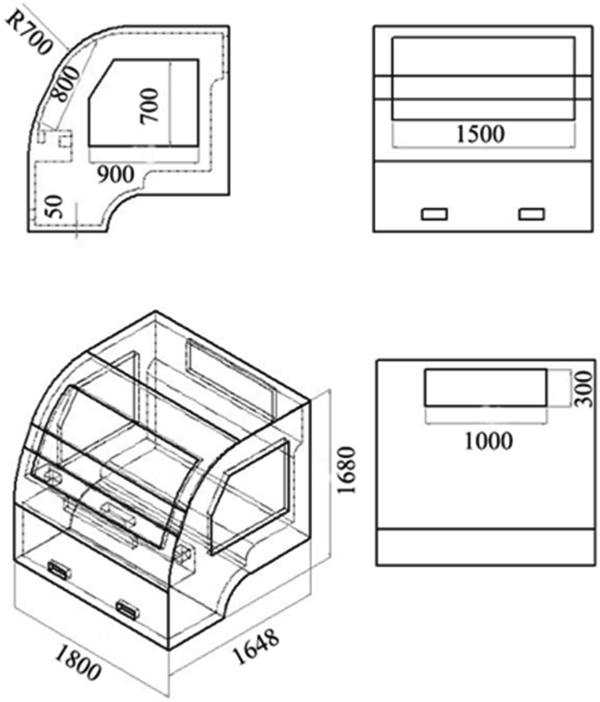

Fig. 4. Geometric dimensions of the truck model used in the present study.

Table 2
Geometric dimensions of the truck model windows.

Glass Position	Length [mm]	Width [mm]	Thickness [mm]	Area [mm^2]
Front	1500	800	5	1 210 000
Side	900	700	5	630 000
Back	1000	300	5	3000

In summary, although there has been a considerable amount of studies conducted on the flow field and the heat environment inside vehicle cabins, there is still a lack of the information of relationships between the external flow and the heat dissipation and condensation of vehicle windows. Moreover, the balance between thermal comfort and dewing problem should also be considered in vehicles. Thus, in the present work numerical simulations were first conducted on the dewing process of an experimental CONAN model to validate the numerical methods, and then the validated methods were applied to study the condensation inside truck cabin to analyze the internal flow distribution and thermal status. By simulating the condensation process, the mechanism of vehicle window dewing process under different air conditions is investigated to achieve an optimal operating state with a combination of the ride comfort and energy consumption efficiency.

Table 3
Physical Parameters of toughened glass.

Material	Density[g/cm^3]	Specific Heat[j/kg·k]	Thermal Conductivity
Glass	2500	720	1.38

2. Methodology

2.1. Numerical simulation details

In this study, the numerical simulations were conducted using the commercial software ANSYS FLUENT 17.0 [33] combined with user defined functions (UDFs) as the main solver. It should be note that the LES (Large Eddy Simulation) method was selected to analyze the turbulence flow around vehicle, and Eulerian Wall Film (EWF) was chosen as the multiphase model. Assuming that the thickness of the liquid film was less than the radius of the wall curvature, the properties of the liquid film in the thickness direction were certain and sufficiently thin to be regarded as the two squares parallel to the wall flow. Accordingly, the basic control equations are as follows [34]:

Mass conservation equation:

$$\frac{\partial h}{\partial t} + \nabla[h\vec{V_l}] = \frac{\dot{m}_s}{\rho_l} \tag{1}$$

where ρ_l is the liquid density, h is the film height, ∇_s is the surface gradient operator, $\vec{V_l}$ is the mean film velocity and $\dot{m}_s$ is the mass source per unit wall area due to droplet collection, film separation, film stripping, and phase change.

Momentum conservation equation:

$$\frac{\partial h\vec{V_l}}{\partial t} + \nabla_s(h\vec{V_l}\vec{V_l}) = -\frac{h\nabla_s P_L}{\rho_l} + (\vec{g_\tau})h + \frac{3}{2\rho_l}\vec{\tau f_s} - \frac{3}{2\rho_l}\vec{V_l} + \frac{\dot{q}}{\rho_l} \tag{2}$$

where P_L is the pressure between gas and liquid, g_τ is the gravity effect in parallel direction of liquid film, τ is the viscous shear force at gas-liquid interface, f_s is the solid surface resistance, V_1 is the viscous force between liquid films and $\dot{q}$ is the momentum source terms for droplet

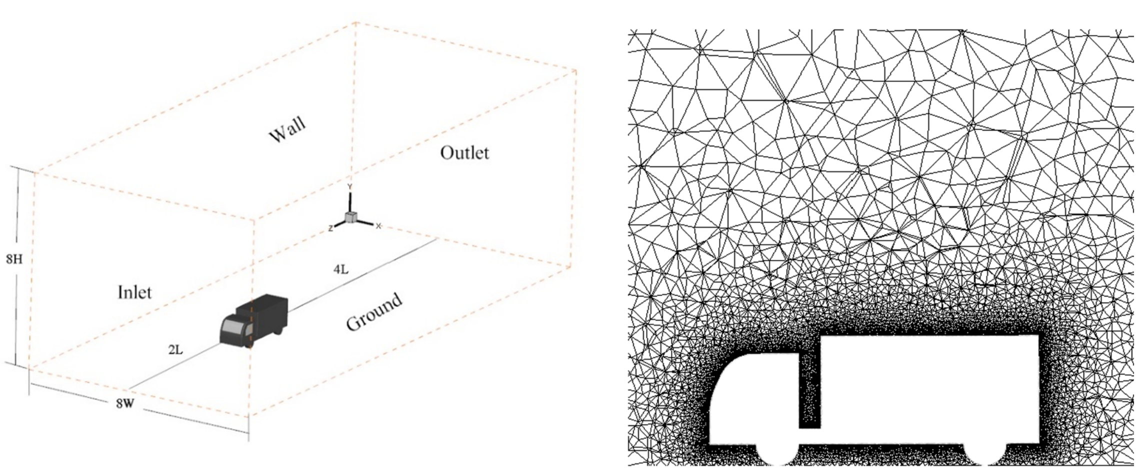

(a) (b)

Fig. 5. Scheme of the simulating model. (a) The computational domain for the external flow field and (b) grids in the Y-Z plane.

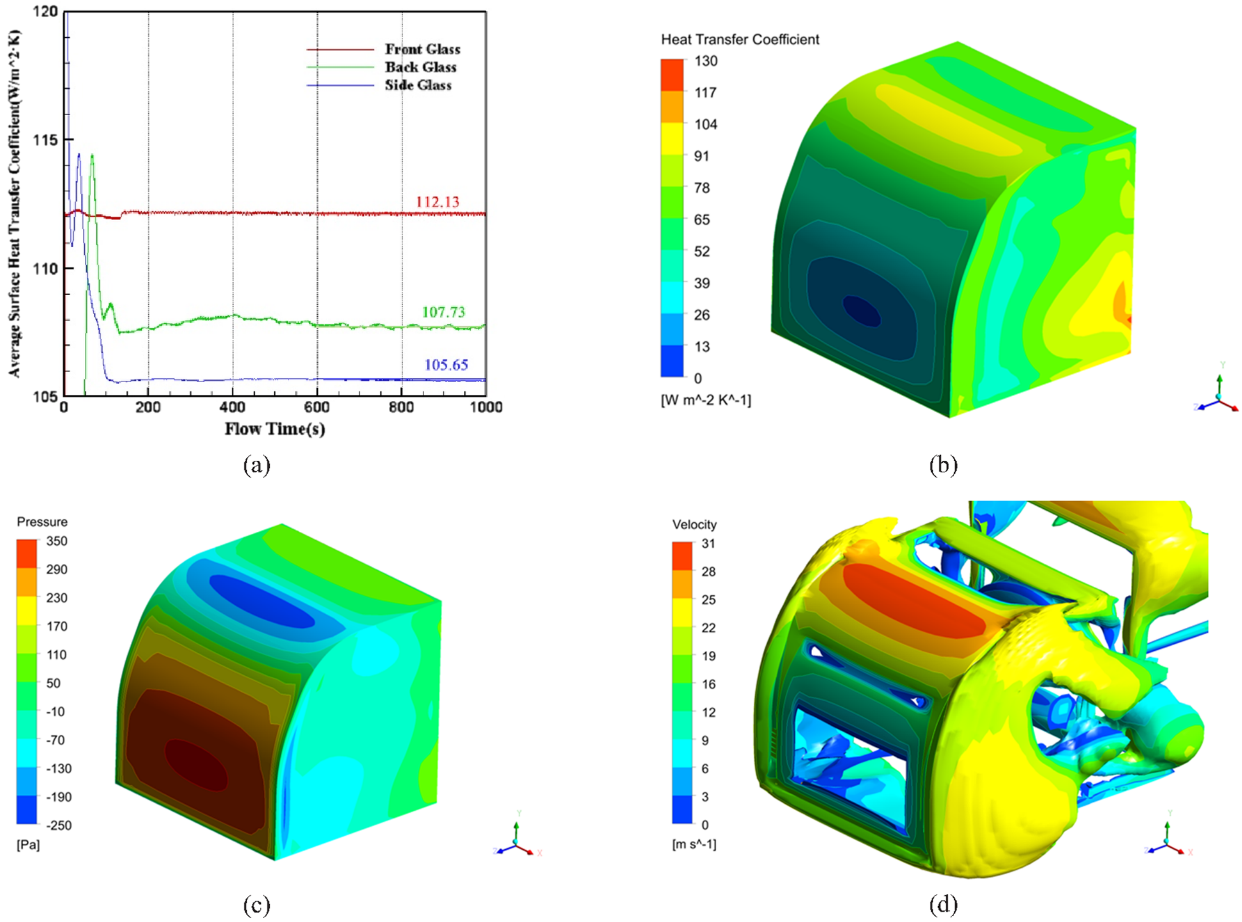

Fig. 6. The heat and flow characters of the cabin. (a) The heat transfer coefficient of the cabin windows. (b) c contours of the heat transfer coefficient of the truck model. (c) The pressure distribution of the truck model. (d) Contours of the external flow velocity field near the exterior wall.

Table 4
Evaluation standard for the indoor thermal comfort.

Season	Temperature[K]	RH[%]	Velocity[m/s]
Summer	295–301	40–65	≤0.3
Winter	292–298	30–60	≤0.2

aggregation or separation.

The left hand of Eq. (2) represents transient and convection effects. On the right hand side, the first term includes the effects of gas-flow pressure, the gravity component normal to the wall surface (known as spreading), and surface tension; the second term represents the effect of gravity in the direction parallel to the film; the third term is the viscous shear force at the gas-film interface; the fourth term represents the viscous force in the film, and the last term is associated with droplet collection or separation. Note that in arriving at the shear and viscous terms on the RHS, a parabolic film velocity profile is assumed.

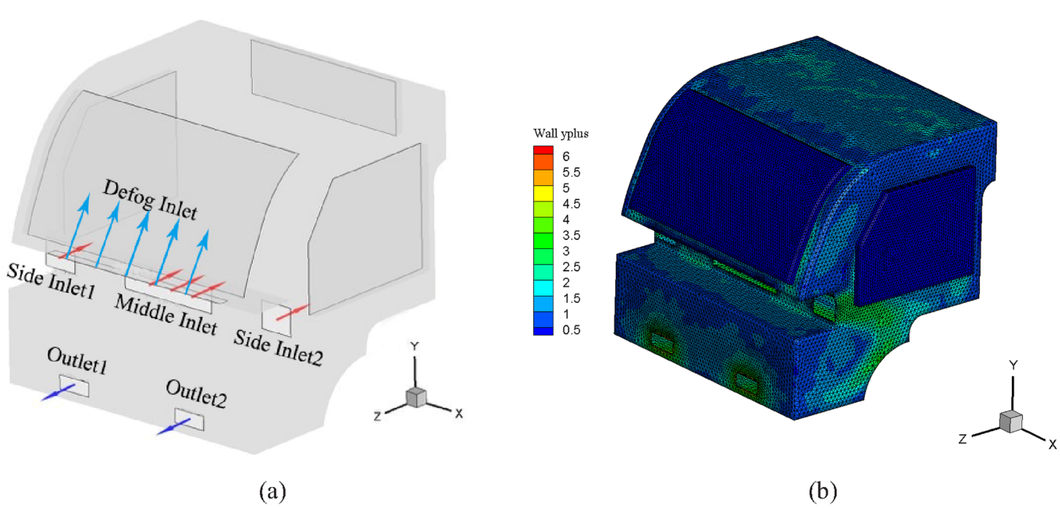

Fig. 7. Computational domain of the internal flow field. (a) scheme of the inlets and outlets; (b) the distribution of y+.

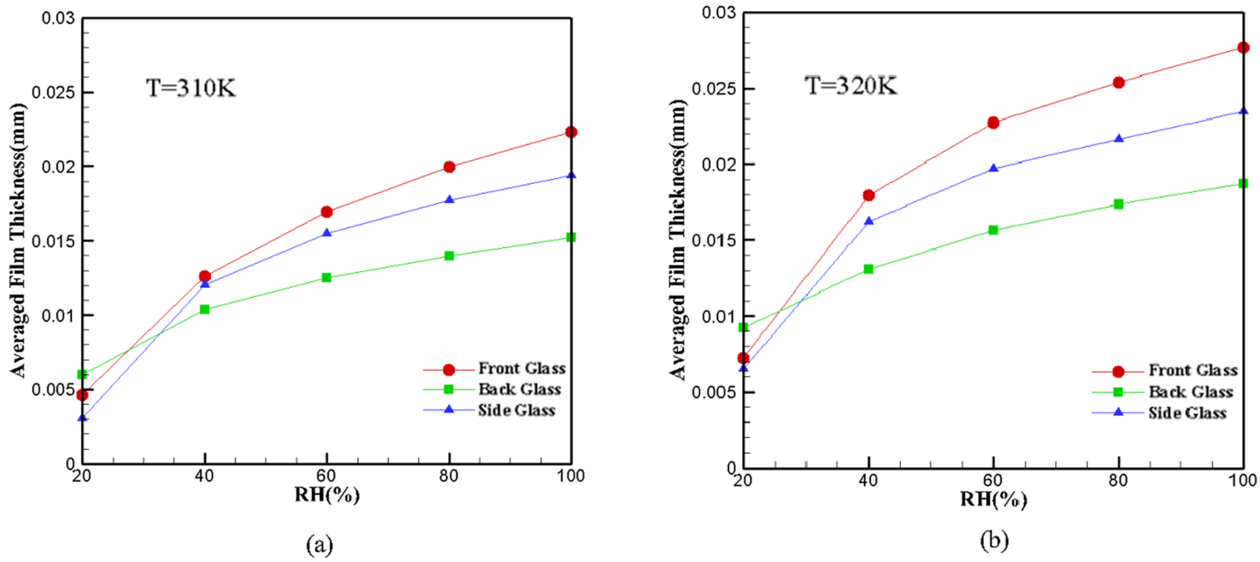

Fig. 8. Variation of the liquid film thickness with the relative humidity at (a) T = 310 K (b) T = 320 K.

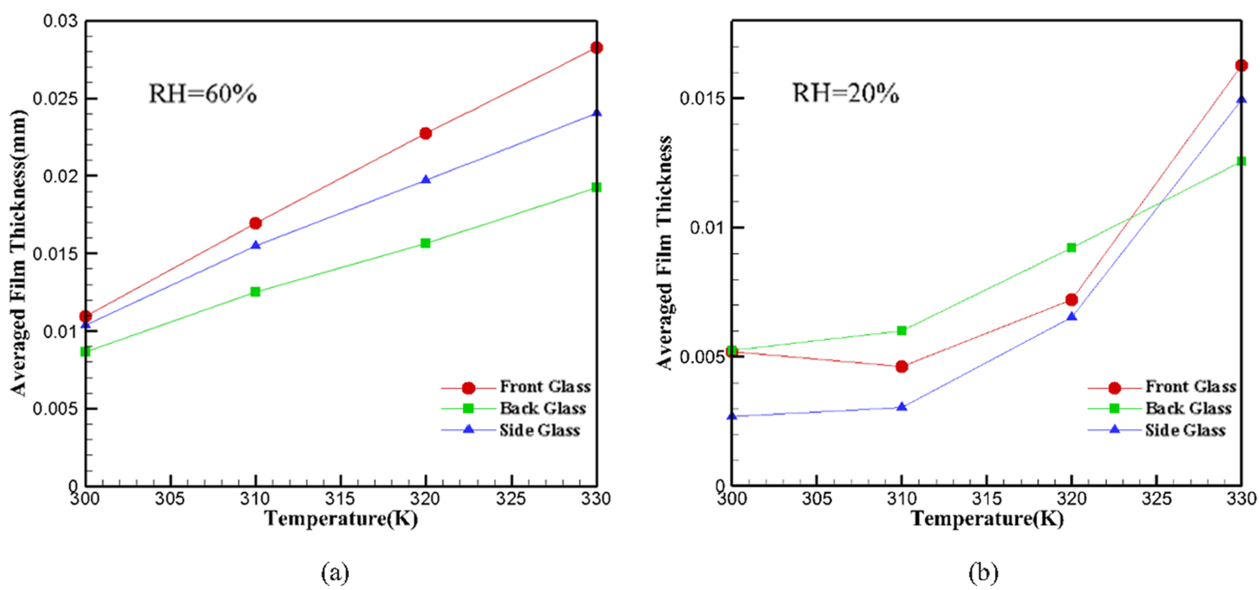

Fig. 9. Variation of the liquid film thickness with the inlet flow temperature at (a) RH = 60% and (b) RH = 20%.

Energy conservation equation:

$$\frac{\partial h\vec{V_l}}{\partial t} + \nabla_s(\vec{V_f}hT_f) = \frac{1}{\rho C_p}\left\{2k_f\left[\frac{T_s + T_w}{h} - \frac{2T_f}{h}\right] + \dot{q}_{imp} + \dot{m}_{vap}L(T_s)\right\} \tag{3}$$

where T_s is temperature at the film-gas interface, T_f is the average film temperature and it is the dependent variable of the above equation, T_w is the wall temperature, $\dot{q}_{imp}$ is the source term due to liquid impingement from the bulk flow to the wall, $\dot{m}_{vap}$ is the mass vaporization or condensation rate, and L is the latent heat associated with the phase change.

In order to analyze the transient process of condensation, UDFs were applied in the present simulations. The water vapor mass fraction is determined by [34]:

$$d = \frac{m_v}{m_a} = \frac{M_v}{M_a} = 0.622\varphi\frac{p_v}{p - p_v} \tag{4}$$

$$\omega = \frac{d}{1 + d} \tag{5}$$

where d is the moisture content, m_v and m_a are the mass of water vapor and air, and M_v and M_a are the molar mass of water vapor and air, respectively; p_v and p are the partial pressure of water vapor and the total pressure, respectively; φ is the relative humidity and ω is the water vapor mass fraction.

Thus, the water vapor diffusion coefficient is given by

$$C_{\text{diff}} = \frac{0.926 \times 10^{-6}}{0.001P}\cdot\frac{T^{2.5}}{T + 245} \tag{6}$$

Saturated pressure of water vapor at a certain temperature:

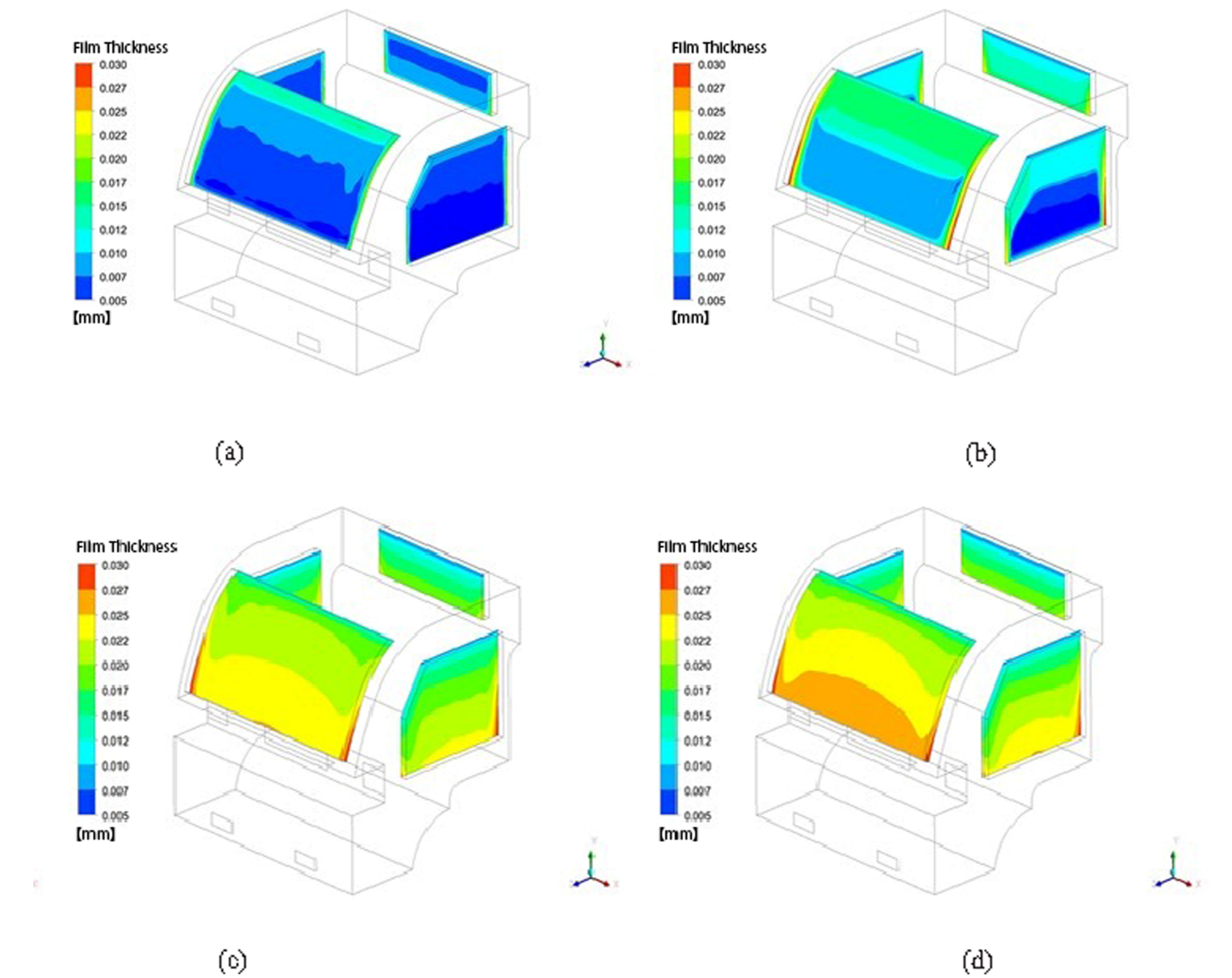

Fig. 10. Evolution of the film thickness contours in the vehicle cabin at (a)100 s (b)300 s (c)700 s (d)1000 s.

$$P_s = \begin{cases} 611.65 + 49.31\cdot T & T < 1 \\ T\cdot(T\cdot(T\cdot(T\cdot(T\cdot(c_5) + c_4) + c_3) + c_2) + c_1) + c_0 + \\ i\cdot(i\cdot(i\cdot(i\cdot(n_4) + n_3) + n_2) + n_1) & T \geqslant 1 \end{cases} \tag{7}$$

where T is the Celsius temperature, $i = \frac{1}{T + 0.001}$, and c_i and n_i are empirical constants, with $n_1 = -0.0111461694$, $n_2 = 0.0110544681$, $n_3 = 0.0014359522$, $n_4 = -0.0111461694$, $c_0 = 0.6141199339$, $c_1 = 0.0440621262$, $c_2 = 0.0014401567$, $c_3 = 0.0000268954$, $c_4 = 0.0000002720$ and $c_5 = 0.0000000028$.

2.2. Validation

To validate the numerical model and UDFs used in this study, the CONAN model used experimentally by Ambrosini et al. (2008) [35] was adopted as the reference for condensation benchmark testing.

Fig. 1 shows the key parameters of the experimental CONAN model of Ambrosini et al. (2008), together with the present numerical finite element model (FEM). In the present FEM, the structured mesh was applied, and the near-wall grids were densified. The nodes number in three direction was 52 × 52 × 120, and the total number of grids was 320,000. It should also be noted that part of the boundary conditions was adopted from the studies of Vyskocil's [36], where the CONAN model was also used as the validation reference. In the present test, the turbulence intensity of inlet was set at 2%; the hydraulic diameter was 0.003 m; pressure of outlet was barometric pressure; the remaining walls were adiabatic; and the acceleration of gravity was 9.81 m/s. Three different experimental inlet parameters were chosen to be simulated, as shown in table 1.

Pressure-based transient calculation method was applied in the simulation. The energy equation was enabled. Standard k-εmodel was used for turbulence model and standard wall function was selected for turbulence model. The EWF model was enabled, together with the mass transfer equation, and the mixture phase is gas water, liquid water and air. The diffusion coefficient and saturated pressure of water vapor was determined by UDFs.

The pressure implicit operator partitioning algorithm (PISO) was used to calculate the pressure. Based on the pressure-velocity coupling relationship, the SIMPLE algorithm was modified to be closer to the real continuity and momentum equation. Pressure, momentum and the spatial discretization of each component were based on the second-

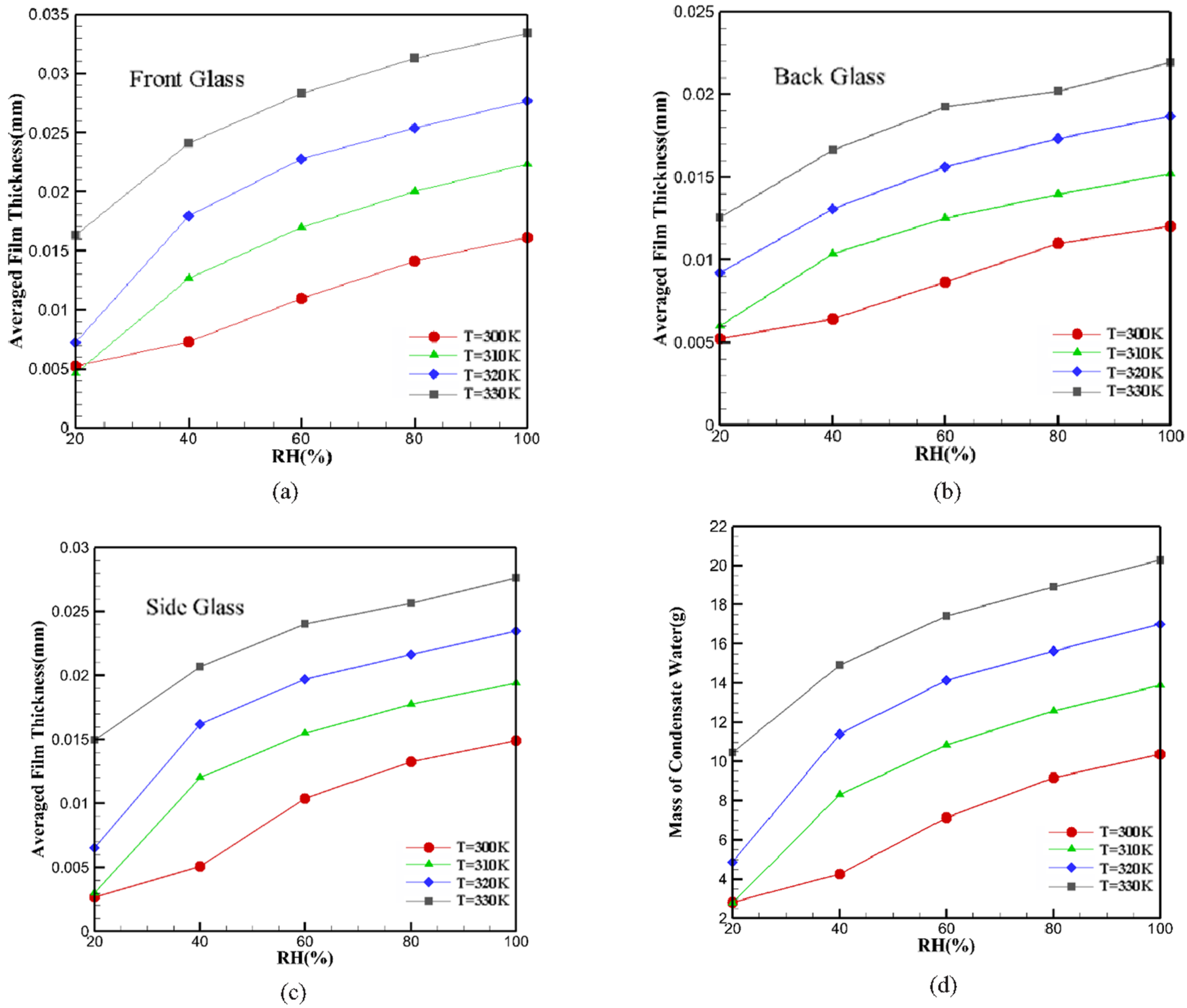

Fig. 11. The Averaged liquid film thickness of (a) front glass (b) back glass (c) side glass and (d) the mass of condensate water in 1000 s of cases with different RH and temperatures.

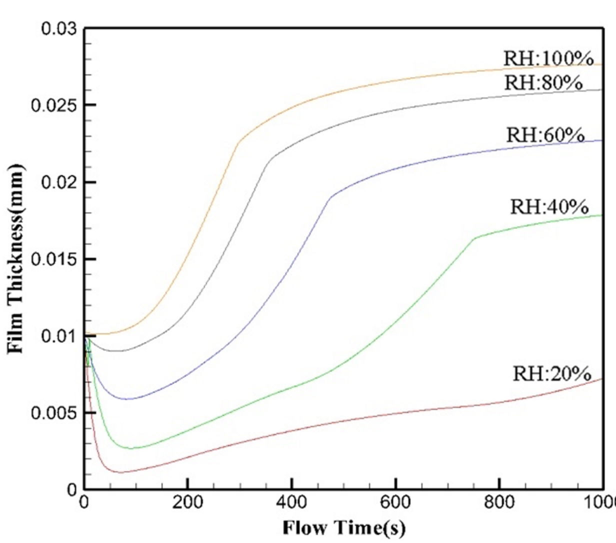

Fig. 12. The Change of Liquid Film Thickness with Time at Different Relative Humidity.

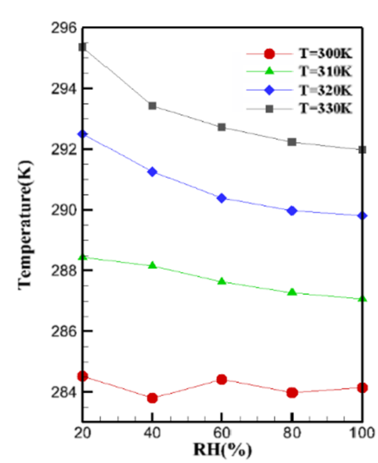

Fig. 13. The relationship between the temperature of the cabin and the temperature and humidity of the inlet.

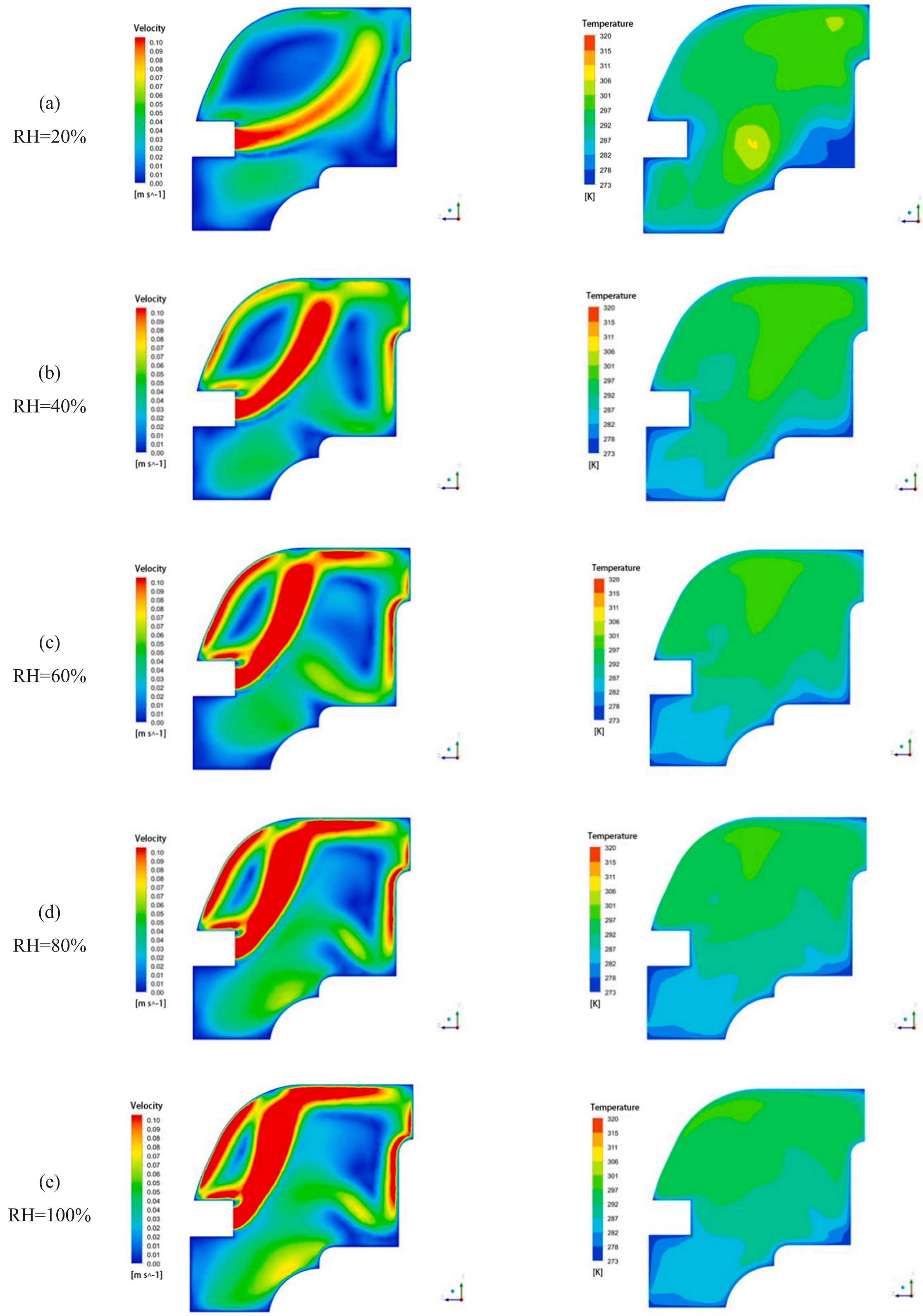

(a) Velocity contours (b) Temperature contours

Fig. 14. The interior flow contours in the center plane and the temperature contours in the ¼ plane for different RH values. The defogging airflow temperature is fixed at 320 K, and the RH = (a) 20% (b) 40% (c) 60% (d) 80% (e) 100%

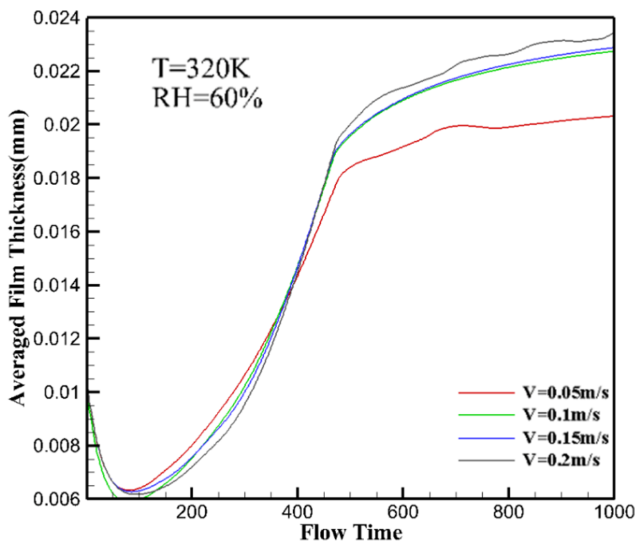

Fig. 15. Change of film thickness with time under different inlet velocities.

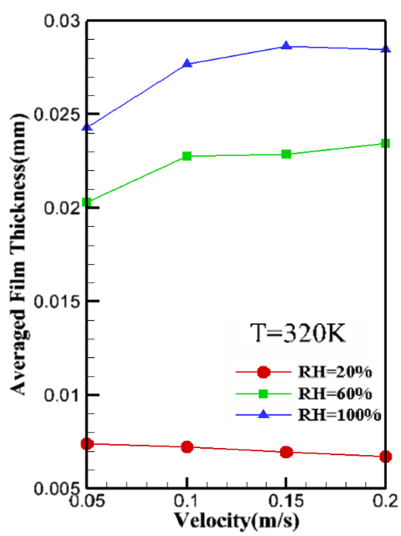

Fig. 16. The relationship between the film thickness and the velocity.

order upwind scheme.

Fig. 2 shows contours of the mass fraction for three different fluids, namely liquid water, gaseous water and air, in the steady state. As can be seen, the liquid water concentrates on the lower part of the cooled plate due to the effect of gravity. The mass fraction of water vapor decreases gradually along the flow direction, while the relative mass fraction of air and liquid water is rising.

Furthermore, comparisons of the heat flux and temperature along the wall (in the X-direction) were made between the present simulations and the previous experiments of Ambrosini [35], as shown in Fig. 3(a) and (b), respectively. It can be seen that the present results in general are in good agreement with the previous experimental measurements, showing the highly similar trends in both the heat flux and the temperature, which first decrease sharply with increases in the distance from the inlet prior to a stable gradually decreasing trend.

3. Discussion on truck model

Considering the complexity and difficulty of the modelling and limited computing resources, we focus here on a simplified truck cabin having relatively simple geometries. In this section, results of the heat transfer coefficient of the vehicle windows and the condensation inside the cabin are presented together with the external and internal flow fields.

3.1. Geometric parameters of truck model

The truck model used in this paper is based on the latest generation of some commercial vehicles, with appropriate simplifications, as shown in Fig. 4. The oversize of the truck head model is 1648 mm × 1800 mm × 1680 mm with four windows (two sides, one front and one rear). The sizes of the windows are shown in table 2.

3.2. Simulation of external flow field

The flow around moving cars is indeed a very complicated problem with profound flow velocity field, turbulence intensity and pressure distribution in different areas around the vehicle body. Thus, large variations in the heat transfer coefficient of different windows may be induced, which can further influence the dewing process on the surface of the windows.

To simulate more accurately the heat transfer process on the vehicle windows, a trailer structure was added based on the original head model (see Yang et al. [37]). The trailer and the truck head had the same dimensions: 4400 mm in length (L), 2000 mm in height (H) and 400 mm in width (W) (the distance between the truck head). The computational domain (4L × 8 W × 8H) was established by ANSYS ICEM, as shown in Fig. 5(a). The inlet was positioned 2L away from the front of the truck, while the outlet was 4L from the rear of the truck. This domain was large enough to eliminate the entrance effect. The unstructured tetrahedral mesh was applied and the grids near the truck body were densified, as shown in Fig. 5(b). The total number of the grid elements was 1.86 million. The transient calculation was adopted. The time step was set to 0.2 s, and total simulation time was 1000 s with 20 iterations for each time step. The calculation method is basically the same as the simulation verification part, choosing Standard $k - \varepsilon$ model as the turbulence model and standard wall function for the near-wall treatment. The inlet flow velocity was set at 20 m/s to simulate the drum of wheels in a real wind tunnel, and the temperature was 273 K, noting that the walls and the ground were adiabatic. The temperature of the four windows was initially set at 283 K. The window material was toughened glass (the physical parameters are shown in table 3).

The surface-averaged heat transfer coefficient of the windows is shown in Fig. 6(a). As can be seen, the heat transfer coefficient in all cases become fairly stable after approximately 200 s, where the differences between different windows are very small, with the highest value observed for the front window, followed by the side and back windows. It should be noted that the average heat transfer coefficients in the stable stage after 600 s were chosen as in the boundary conditions for the simulations of condensation which will be presented.

Furthermore, Fig. 6(b), (c) and (d) show contours of the heat transfer coefficient and the pressure on the body surfaces, and the external flow velocity field, respectively. The minimum value of the heat transfer coefficient observed is in the lower part of the truck head where the heat transfer is directly impacted by the highest pressure and almost zero flow velocity. On the other hand, the highest heat transfer coefficient value occurs at the top of the truck head where the airflow displays the highest velocity and the flow separates. Moreover, the heat

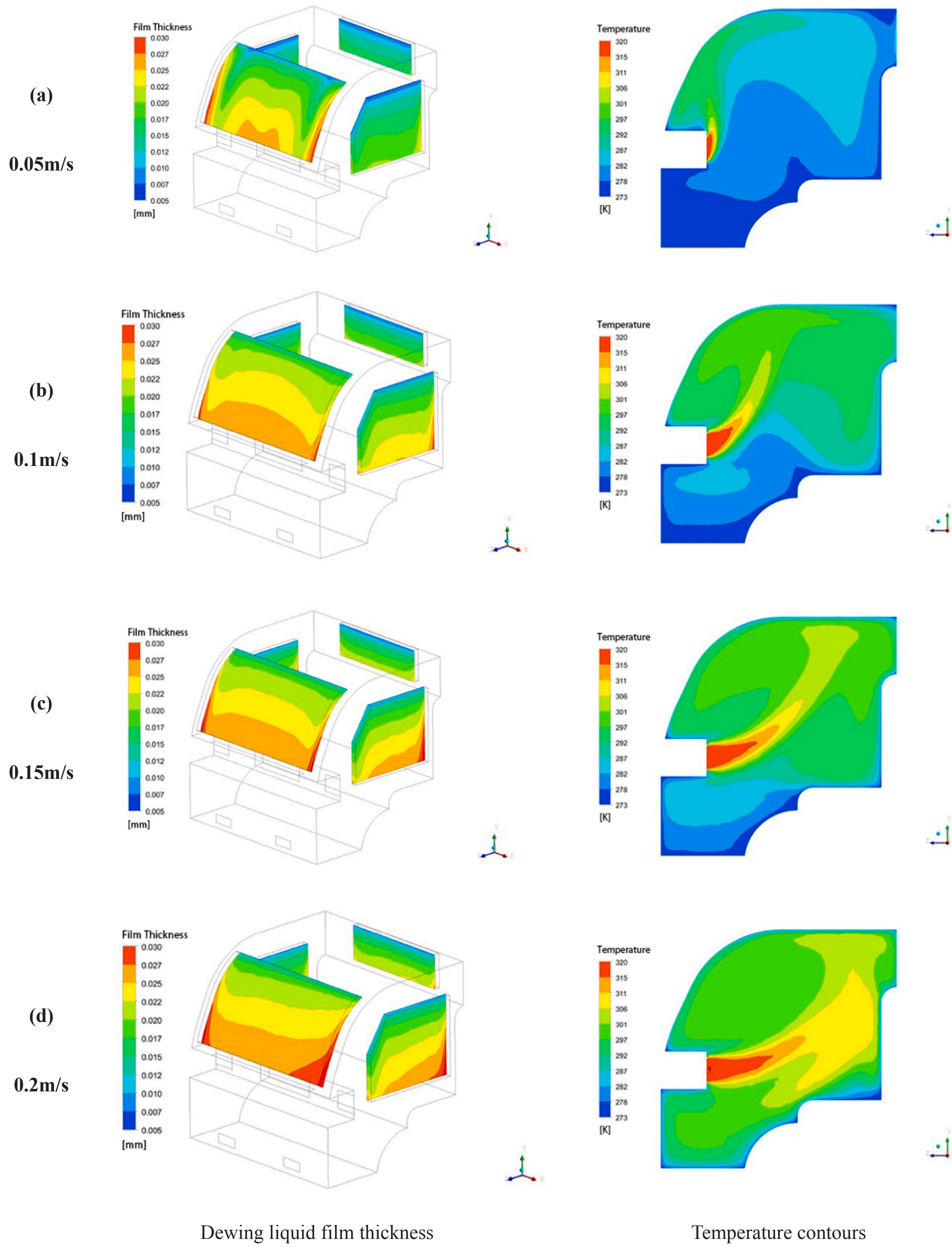

Fig. 17. Contours of the dewing liquid film thickness in glassed and temperature contours in the centerplane when the inlet velocity is (a) 0.05 m/s (b) 0.1 m/s (c) 0.15 m/s (d) 0.2 m/s.

transfer coefficient of the front window, in general, is slightly higher than that of the side and rear windows. Therefore, it can be concluded that the heat transfer coefficient is strongly related to the local flow velocity and pressure distribution.

3.3. Dewing progress and analysis

3.3.1. Evaluation standard for the indoor thermal comfort

In addition to the dewing phenomenon, the thermal comfort of occupants in the vehicle is also of our concern in this article. The standard of indoor thermal comfort is based on '*Code for Design of*

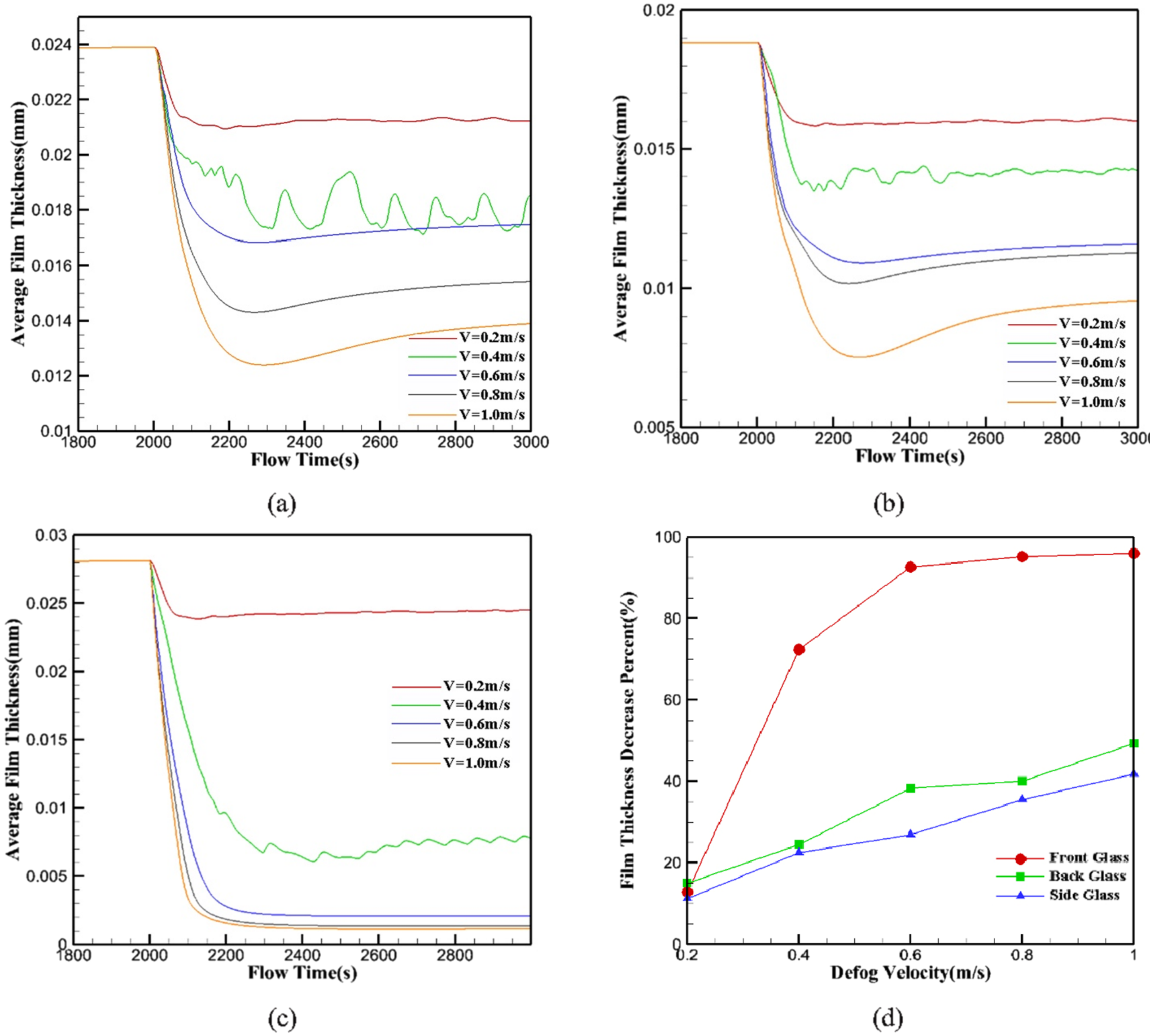

Fig. 18. The change of film thickness with time under different defog velocities at (a) front glass (b) back glass (c) side glass, and (d) the drop percentage of film under different defog velocities.

Heating Ventilation and Air Conditioning' (GB50019-2003) shown in table 4.

3.3.2. Computational domain

The computational domain used for the indoor thermal comfort study is shown in Fig. 7 (a). There are four inlets, including the main inlet (with a cross-sectional area of 960 mm^2), two side inlet (with a cross-sectional area of 960 mm^2), and a special defog inlet (with a cross-sectional area of 400 mm^2) which is set below the front window. The two outlets (with a cross-sectional area of 160 mm^2) are located below the control panel. The main inlet is located in the middle of the control panel and two smaller inlets are on each side of the cabin, while two outlets are located under the control panel, close to the driver's feet position according to actual structure.

Considering the complex shape of the model, an unstructured tetrahedral mesh was used. To ensure better condensation effects, the window entity was retained. The y-plus value is a dimensionless wall distance to reflect the mesh quality and we generally choose the value smaller than 3–5 as the criterion of good mesh quality. The y-plus value of the window is approximately 0.5 and the distribution is shown in Fig. 7(b), fully satisfying the mesh quality requirement.

3.3.3. Simulation conditions

To gain a better understanding of the system, various inlet flow conditions, i.e., the inlet type, the flow velocity, the relative humidity and the temperature, were tested. This resulted in a total of 36 test cases (for more details, refer to Table 1 in Appendix). The transient simulation method was adopted, where most settings were kept the same as in the validation test and chose Standard $k-\varepsilon$ model as the turbulence model and standard wall function for the near-wall treatment. The initial temperature in the cabin was unified and set at 288 K. The averaged heat transfer coefficient obtained in Section 3.2 section was used

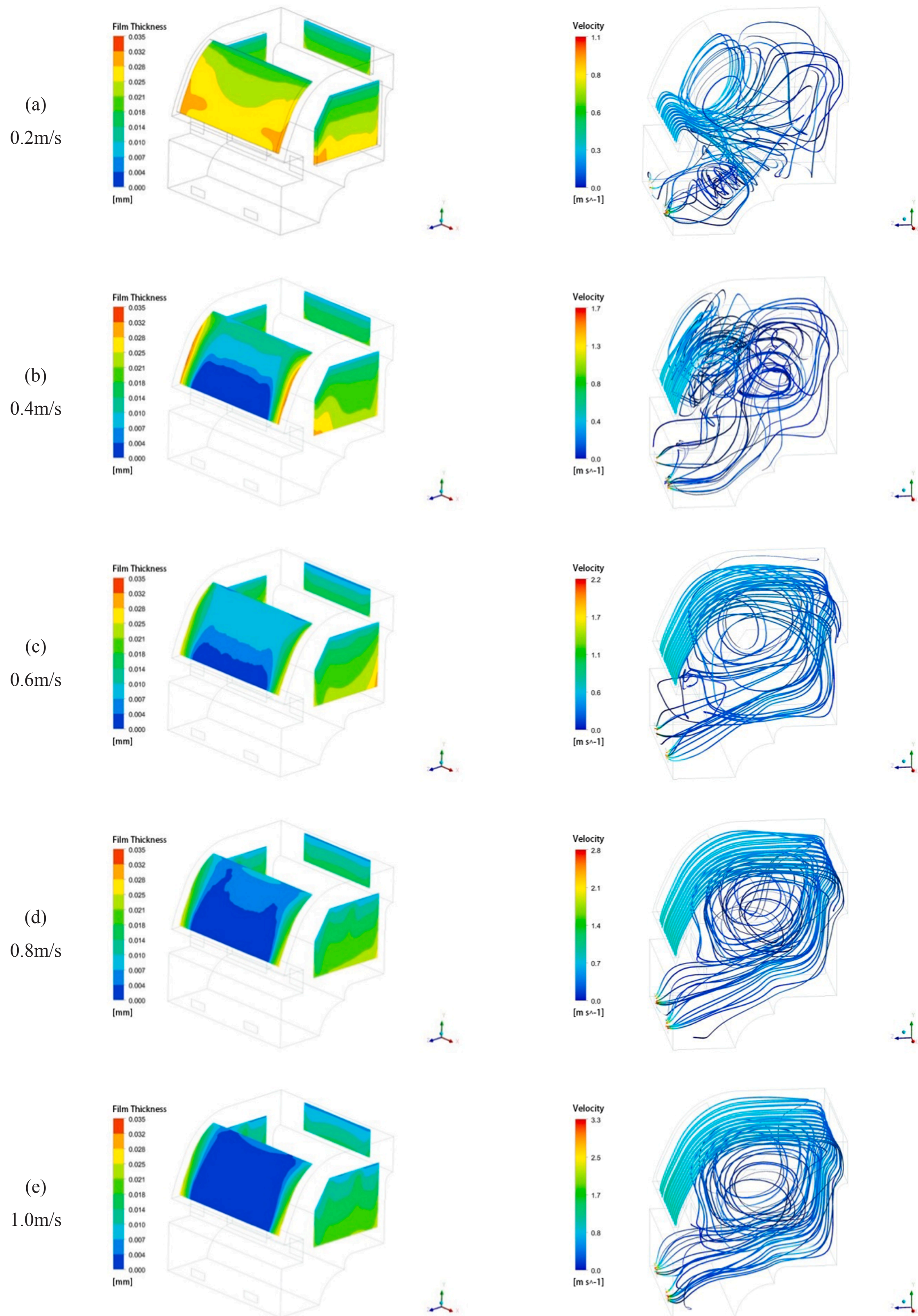

Fig. 19. The film contours and velocity streamlines in 100 s when defog velocity at (a) 0.2 m/s (b) 0.4 m/s (c) 0.6 m/s (d) 0.8 m/s and (e) 1.0 m/s.

as the input condition. The initial thickness of water film was set to 0.01 mm to ensure that the cabin had certain humidity to achieve a faster condensation process.

3.3.4. Condensation at different positions of the cabin windows

It has been known that the dewing liquid film thickness on different windows are noticeably different. Fig. 8 shows the variation of the averaged film thickness at 1000 s with the relative humidity (RH) for the cabin windows with fixed inlet flow temperature values of

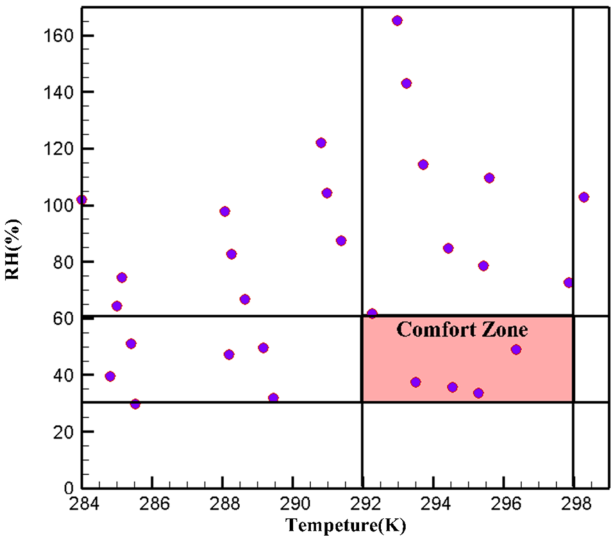

Fig. 20. Distribution of the cabin temperature and RH for all the test cases at 1000 s.

T = 310 K and 320 K (cases 13–22). As can be seen, the variations of the liquid film thickness with RH are very similar in the two fixed temperature cases. It should be noted that the film thickness tends to increase with the inlet flow temperature.

Fig. 9 presents the variation of the averaged film thickness at 1000 s with the inlet flow temperature at two fixed relative humidity values of RH = 60% and 20%. For RH = 60%, the film thickness increases linearly with the inlet flow temperature in all the window cases. The font window exhibits the greatest film thickness and the fastest increasing rate. For RH = 20%, the film thickness of all the window cases increases marginally for T < 320 K, prior to a rapid increasing trend; however, the overall film thickness is relatively thin (close to the initial thickness of 0.01 mm), indicating that low humidity results in slow condensation.

Furthermore, one representative case with T = 320 K and RH = 60% (case 15) was selected to demonstrate the evolution of the dewing process. Fig. 10 shows the film thickness contours at four different time instances, t = 100 s, 300 s, 700 s and 1000 s. It can be seen that the condensation of the front and side windows starts from the top, while the rear window begins to dew from the bottom. At t = 1000 s when the condensation becomes saturated, the highest value appears at the lower part of the front window. It should also be noted that the condensation of the windshield window in general appears to be more severe than the side and rear windows. One primary factor for this seems to be the distance from the air-conditioning inlet. The results indicate that the front window can be used as an important object for analyzing the influence of the temperature and humidity on the condensation.

3.3.5. Influence of the temperature and humidity

The temperature and humidity are two main factors in the analysis of condensation mechanism in this study. Fig. 11(a–c) shows the variations of the film thickness with RH for different fixed temperature values at t = 1000 s, while Fig. 11(d) shows the variation of the mass of condensate water correspondingly. Clearly, these plots all show that increases in the temperature and humidity lead to aggravations in condensation. In other words, the effect of moisture on condensation gradually reduces as the relative humidity is increased. On the other hand, in general, increasing the temperature on condensation is of more significance.

Fig. 12 presents the time evolution of the film thickness of the front window with a fixed temperature of 320 K and different RH values. Clearly, the higher the relative humidity is, the higher the thickness of the liquid film and the faster the condensation rate will be, and the stability will be achieved earlier. Moreover, Fig. 13 plots the averaged temperature inside the cabin as a function of RH. As can be seen, the averaged temperature in the cabin decreases marginally as RH is increased. However, when the inlet temperature is lower close to the cabin temperature, the influence of RH on the temperature in the cabin is not obvious anymore.

To further evaluate the driver's thermal comfort, Fig. 14 shows the flow velocity contours in the center plane with five different RH values at fixed inlet temperature 320 K, together with the resulted temperature contours in the ¼ plane (corresponding to the driver's position). As can be seen, increasing RH sees a stronger and larger flow field forming on the windshield window. This is most likely due to the increase in the water vapor mass fraction and the decrease in the air density making the air flow to roll up easier.

From the temperature contours, when RH is below 20%, the areas close to the driver's head and leg can achieve an excellent warmth effect, with a temperature of approximately 297 K. As the humidity is increased, the high-temperature region shrinks gradually, and tends to shift from the diver's head position towards the front window. In the extreme cases with RH = 20%, the high-temperature region is reduced to a small area around the upper part of the front window, implying that the upper body of the driver is not warmed effectively, while the temperature around the position of the driver's legs is even lower than the initial temperature (288 K). From the above results, it can be concluded that increasing relative humidity can cause the internal airflows to roll up faster towards the front window and thus the warm-temperature region moves towards the upper part of the cabin, which is not effective for the occupants' thermal comfort. Thus, it is suggested that the relative humidity is an important factor to be considered in the vehicle air-conditioning design.

3.3.6. Influence of the inlet velocity

The distribution of condensation and temperature and humidity under four different inlet velocity is analyzed in this section. Fig. 15 is the change of front window's film thickness with time of cases with different inlet velocity in 320 K and RH60%. The basic trend of four curves is almost the same, while the final thickness increases with the rising of velocity. In the case of 0.05 m/s, the final thickness is obviously lower than other conditions and fluctuation occurs in cases of 0.05 m/s and 0.2 m/s. Fig. 16 shows the relationship between final film thickness and velocity in different RH conditions. In RH 60% and 100%, there is a positive relation between the thickness of the film and the velocity. In cases of RH 20%, there is no obvious difference of thickness at different velocity and it has a slightly decreasing trend with the increase of inlet velocity.

Fig. 17 displays the contours of film thickness and the temperature distribution in different inlet velocity. At the velocity of 0.05 m/s, the air flows from the vent only a small distance and then flows upward, so the area near front window is strongly warmed and thus leads to the relatively lower film thickness. The highest thickness of the front window film is located in the middle of the lower part and the thickness of the liquid film on both sides is obviously lower. With the increase of wind speed, the thickness of liquid film is distributed even more evenly in the horizontal direction and the two sides are also in the area with the highest thickness of the liquid film. Under the high velocity of 0.2 m/s, the flow is rather disorder and results in the fluctuation of curves in Fig. 15. The distribution of the film thickness turns to be asymmetrical.

Considering the heating effect, the diver's position is far below the comfort temperature in cases of 0.05 m/s, while the temperature in cases of 0.1 m/s and 0.15 m/s is more suitable and the temperature around area of the driver's head is about 295 K. The temperature is excessive in cases of 0.2 m/s which is over 300 K that beyond the comfort temperature.

3.3.7. Influence of the defog flow and parameters

On the base of the case in last section, the defogging inlet which is located below the front window was opened at 2000 s and different inlet velocities were simulated. The mass fraction of air from defog inlet was set to 0 and the temperature is 320 K with 5 different velocities shown in Table 1 in Appendix (cases 3–7). The change of film thickness of each window with time under different velocities is shown in Fig. 18. Fig. 18(a-c) plot the change of film thickness for three different windows, while Fig. 18(d) evaluates the reduction percentage of the water film.

It could be noticed from these four pictures that the opening of defogging inlet could remove the dew on windows effectively. The best defogging effect is achieved when defogging is operated for approximately 200 s when the water film was reduced to lowest. Keeping the defogging inlet open for too long may increase the film thickness on the back and side windows, rather than reducing the thickness of the film.

As indicated in Fig. 18(d), the defogging effect is mostly obvious for the front window, while much less effects are seen on the side window and back windows. The fog removal rate increases rapidly with the increase of the velocity of inlet. However, when the velocity reaches a certain speed, the fog removal rate becomes limited. When the velocity of the defog inlet reaches 0.6 m/s, the defogging effect of the front window is basically the highest and the film thickness will not decrease further with the increase of the velocity.

Fig. 19 shows the contours of film thickness at $t = 100$ s and the velocity streamlines inside the cabin with different inlet velocities. The effect of inlet velocity on defogging is obvious. With the increase of velocity, the thickness drops, and defogging speed is significantly strengthened. For the velocity at 0.2 m/s, the airflow from the inlet rises and then begins to fall back such that it cannot cover the front window surface at all and therefore has poor defogging performance. While in cases at 0.4 m/s, where the film thickness fluctuates largely, the airflow first rises to the middle of front window and then starts to fall and intertwines with airflow from other inlet, and the whole flow field is quite disorder. The disorder of air flow causes the unstable distribution of water gas which could be the main reason that leads to the fluctuation of film thickness. For the cases of airflow velocity ≥ 0.6 m/s, the air can flow steadily through the whole front window and the top of cabin, and thus form a large stable eddy current in the cabin. In this case, the flow field and moisture distribution in the cabin is more stable.

In conclusion, the defog inlet has a significant effect on diminishing dew on the front window. It was found that the optimum defogging airflow velocity was 0.6 m/s, with which the most effective defogging was achieved with significant energy saving. It was also found that the effective defogging effect could be reached after opening the inlet for 100 s; however, longer operation time may result in adverse effects to cause increases in the film thickness, and also cause overheating that adversely affects driving comfort in the cabin.

3.4. An overall evaluation

In this section, an overall assessment of all cases tested in this study, by considering the condensation, the thermal comfort standard of temperature and humidity in the cabin, and the economic efficiency synthetically.

Fig. 20 presents the distribution of all the test cases in the plane of the temperature and relative humidity. As highlighted in red, four cases (12, 17, 29 and 30 in table 5) fall in the comfort zone (30% < RH < 60% and 292 K < T < 298 K) at 1000 s, which would be useful to provide references for the future design of vehicular air conditioning systems.

4. Conclusions

This paper has numerically studied the dewing phenomenon and defogging progress of a truck cabin model. By comparing with previous experimental results of CONAN model, the EWF model combined with UDF was validated to be successfully in simulating the dewing problem. Then the study was focused on the dewing phenomenon of a truck cabin, where the heat dissipation of window glasses was considered by simulating the external flow field. A total of 33 different working conditions with different temperature and relative humidity of air-condition system flow velocities were simulated to better understand the development of dewing film. The defogging airflow was also discussed with different flow velocities to evaluate the defogging performance.

It was found through the external flow velocity field, the convective heat transfer coefficient of the front window was higher than that of the side and back windows. This is most likely due to the differences in the external flow velocity around different parts of the cabin surfaces.

The temperature and humidity in the cabin are two important factors in the condensation process of the windows. The present results showed that reducing the humidity could not only effectively control the condensation, but also optimize the distribution of the internal airflow and increase the heating effect. On the other hand, low cabin temperature affects the occupants' thermal comfort, whereas high temperature will increase the content of water vapor in the cabin, thereby worsening the problem of condensation.

The defogging airflow velocity was found to have a significant impact on the liquid film thickness. When the defogging airflow velocity was greater than 0.6 m/s, the dews on the front window was diminished rapidly. In addition, the operation time of the demister should be approximately 200 s to achieve desired defogging effects; otherwise, longer operation time may result in not only inefficient energy consumption, but also excessive temperature rises adversely affecting the occupants' comfort in the cabin.

To satisfy the comfortable (proper temperature), efficiency (lower velocity with lower fan energy consumption), and safety (thin film) requirements in the same time, this paper suggests that the automobile air conditioner could be controlled within the relative humidity range of 20% < RH < 60% and the temperature range of 292 K < T < 298 K.

Declaration of Competing Interest

On behalf of all the co-authors of the submitted paper, I can confirm that we have no financial and personal relationships with other people or organizations that can inappropriately influence our work, there is no professional or other personal interest of any nature or kind in any product, service and/or company that could be construed as influencing the position presented in, or the review of, the manuscript entitled, 'Optimization of the automotive air conditioning strategy based on the study of dewing phenomenon and defogging progress'.

Acknowledgements

This study is supported by National Natural Science Foundation of China under grants No. 51206141 and 91741203.

Appendix A

This article studied a large number of cases with various combinations of different parameters, this table was designed to introduce these cases better and make it easier to discuss the influence of these parameters in the following sections (See Table A1).

Table A1
Inlet conditions for all the test cases in the present study.

Cases	Inlet Parameters				
	Velocity [m/s]	Temperature [K]	RH[%]	ω_{vap}	Inlet Types
(1) V1-T320-H100-1	0.1	320	100	0.0679	Middle
(2) V1-T320-H100-3	0.1	320	100	0.0679	Middle-Side
(3) V2-T320-H100-4	0.2	320	100	0.0679	Defog
(4) V4-T320-H100-4	0.4	320	100	0.0679	Defog
(5) V6-T320-H100-4	0.6	320	100	0.0679	Defog
(5) V8-T320-H100-4	0.8	320	100	0.0679	Defog
(7) V10-T320-H100-4	1	320	100	0.0679	Defog
(8) V1-T330-H100-3	0.1	330	100	0.1173	Middle-Side
(9) V1-T330-H80-3	0.1	330	80	0.0961	Middle-Side
(10) V1-T330-H60-3	0.1	330	60	0.0739	Middle-Side
(11) V1-T330-H40-3	0.1	330	40	0.0532	Middle-Side
(12) V1-T330-H20-3	0.1	330	20	0.0259	Middle-Side
(13) V1-T320-H100-3	0.1	320	100	0.0679	Middle-Side
(14) V1-T320-H80-3	0.1	320	80	0.0551	Middle-Side
(15) V1-T320-H60-3	0.1	320	60	0.0419	Middle-Side
(16) V1-T320-H40-3	0.1	320	40	0.0291	Middle-Side
(17) V1-T320-H20-3	0.1	320	20	0.0144	Middle-Side
(18) V1-T310-H100-3	0.1	310	100	0.0409	Middle-Side
(19) V1-T310-H80-3	0.1	310	80	0.0330	Middle-Side
(20) V1-T310-H60-3	0.1	310	60	0.0249	Middle-Side
(21) V1-T310-H40-3	0.1	310	40	0.0167	Middle-Side
(22) V1-T310-H20-3	0.1	310	20	0.0085	Middle-Side
(23) V1-T300-H100-3	0.1	300	100	0.0222	Middle-Side
(24) V1-T300-H80-3	0.1	300	80	0.0179	Middle-Side
(25) V1-T300-H60-3	0.1	300	60	0.0135	Middle-Side
(26) V1-T300-H40-3	0.1	300	40	0.0090	Middle-Side
(27) V1-T300-H20-3	0.1	300	20	0.0045	Middle-Side
(28) V0.5-T320-H20	0.05	320	20	0.0144	Middle-Side
(29) V1.5-T320-H20	0.15	320	20	0.0144	Middle-Side
(30) V2-T320-H20	0.2	320	20	0.0144	Middle-Side
(31) V0.5-T320-H60	0.05	320	60	0.0419	Middle-Side
(32) V1.5-T320-H60	0.15	320	60	0.0419	Middle-Side
(33) V2-T320-H60	0.2	320	60	0.0419	Middle-Side
(34) V0.5-T320-H100	0.05	320	100	0.0679	Middle-Side
(35) V1.5-T320-H100	0.15	320	100	0.0679	Middle-Side
(36) V2-T320-H100	0.2	320	100	0.0679	Middle-Side

V-velocity T-temperature H-relative humidity and the last number represents the number of inlets.

Appendix B. Supplementary material

Supplementary data to this article can be found online at https://doi.org/10.1016/j.applthermaleng.2020.114932.

References

[1] E. Sterling, A. Arundel, T. Sterling, Criteria for human exposure to humidity in occupied buildings, ASHRAE Trans. B 91 (1985) 611–622.
[2] L. Kai, W. Enlu, Deli Li, Numerical and experimental investigation on water vapor condensation in turbulent flue gas, Appl. Therm. Eng. 160 (2019) 114009, , https://doi.org/10.1016/j.applthermaleng.2019.114009.
[3] J. Serrano, P. Piqueras, R. Navarro, D. Tarí, C. Meano, Development and verification of an in-flow water condensation model for 3D-CFD simulations of humid air streams mixing, Comput. Fluids 167 (2018) 158–165, https://doi.org/10.1016/j.compfluid.2018.02.032.
[4] Q. Yi, M. Tian, W. Yan, X. Qu, X. Chen, Visualization study of the influence of non-condensable gas on steam condensation heat transfer, Appl. Therm. Eng. 106 (2016) 13–21, https://doi.org/10.1016/j.applthermaleng.2016.05.134.
[5] M. Ghafari, M. Ghofrani, F. Dauria, New turbulence modeling for simulation of Direct Contact Condensation in two-phase pressurized thermal shock, Prog. Nucl. Energy 108 (2018) 358–371, https://doi.org/10.1016/j.pnucene.2018.06.007.
[6] A. Palmowska, B. Lipska, Experimental study and numerical prediction of thermal and humidity conditions in the ventilated ice rink arena, Build. Environ. 108 (2016) 171–182, https://doi.org/10.1016/j.buildenv.2016.08.024.
[7] A. Palmowska, B. Lipska, Research on improving thermal and humidity conditions in a ventilated ice rink arena using a validated CFD model, Int. J. Refrig. 86 (2018) 373–387, https://doi.org/10.1016/j.ijrefrig.2017.11.016.
[8] A. Dehbi, F. Janasz, B. Bell, Prediction of steam condensation in the presence of noncondensable gases using a CFD-based approach, Nucl. Eng. Des. 258 (2013) 199–210, https://doi.org/10.1016/j.nucengdes.2013.02.002.
[9] G. Zschaeck, T. Frank, A. Burns, CFD modelling and validation of wall condensation in the presence of non-condensable gases, Nucl. Eng. Des. 279 (2014) 137–146, https://doi.org/10.1016/j.nucengdes.2014.03.007.
[10] P. Birbarah, N. Miljkovic, Internal convective jumping-droplet condensation in tubes, Int. J. Heat Mass Transf. 114 (2017) 1025–1036, https://doi.org/10.1016/j.ijheatmasstransfer.2017.06.122.
[11] U. Kleinhans, R. Rück, S. Schmid, T. Haselsteiner, H. Spliethoff, Alkali vapor condensation on heat exchanging surfaces: laboratory-scale experiments and a mechanistic CFD modeling approach, Energy Fuels 30 (11) (2016) 9793–9800, https://doi.org/10.1021/acs.energyfuels.6b01658.
[12] T. Phan, S. Won, W. Park, Numerical simulation of air–steam mixture condensation flows in a vertical tube, Int. J. Heat Mass Transf. 127 (2018) 568–578, https://doi.org/10.1016/j.ijheatmasstransfer.2018.08.043.
[13] J. Liu, H. Aizawa, H. Yoshino, CFD prediction of surface condensation on walls and its experimental validation, Build. Environ. 39 (8) (2004) 905–911, https://doi.org/10.1016/j.buildenv.2004.01.015.
[14] M.T. Bourhan, A.A. Moh'd, A.K. Mohammad, A comprehensive review of ejector design, performance, and applications, Appl. Energy 240 (2019) 138–172, https://doi.org/10.1016/j.apenergy.2019.01.185.

[15] P. He, B. Zhang, C. Zhu, Z. Ji, C. Lin, Dynamic process modeling on depressurization by cooling-controlled condensation in a closed chamber, Int. J. Heat Mass Transf. 78 (2014) 330–340, https://doi.org/10.1016/j.ijheatmasstransfer.2014.06.049.
[16] J. Hara, K. Fujitani, K. Kuwahara, Computer simulation of passenger compartment airflow, SAE Technical Paper Series (1988), https://doi.org/10.4271/881749.
[17] S. You, W. Li, T. Ye, F. Hu, W. Zheng, Study on moisture condensation on the interior surface of buildings in high humidity climate, Build. Environ. 125 (2017) 39–48, https://doi.org/10.1016/j.buildenv.2017.08.041.
[18] S. Somnath, S. Mayur, Numerical simulation and validation of cabin aiming and cool-down of a passenger car. SAE Technical Paper Series, 2016. doi: http://doi.org/10.4271/2016-01-0251.
[19] K. Saboora, M. Kim, Human thermal comfort and heat removal efficiency for ventilation variants in passenger cars, Energies 10 (11) (2017) 1710, https://doi.org/10.3390/en10111710.
[20] M. Oh, J. Ahn, D. Kim, D. Jang, Y. Kim, Thermal comfort and energy saving in a vehicle compartment using a localized air-conditioning system, Appl. Energy 133 (2014) 14–21, https://doi.org/10.1016/j.apenergy.2014.07.089.
[21] S. Schaut, O. Sawodny, Thermal management for the cabin of a battery electric vehicle considering passengers' comfort, IEEE Trans. Control Syst. Technol. 1–17 (2019), https://doi.org/10.1109/tcst.2019.2914888.
[22] Z. Zhang, C. Liu, X. Chen, C. Zhang, J. Chen, Annual energy consumption of electric vehicle air conditioning in China, Appl. Therm. Eng. 125 (2017) 567–574, https://doi.org/10.1016/j.applthermaleng.2017.07.032.
[23] Huajun Zhang, Lan Dai, Guoquan Xu, Yong Li, Wei Chen, Wenquan Tao, Studies of air-flow and temperature fields inside a passenger compartment for improving thermal comfort and saving energy. Part II: Simulation results and discussion, Appl. Therm. Eng. 29 (2009) 2028–2036, https://doi.org/10.1016/j.applthermaleng.2008.10.006.
[24] P. Danca, A. Vartires, A. Dogeanu, An overview of current methods for thermal comfort assessment in vehicle cabin, Energy Procedia 85 (2016) 162–169, https://doi.org/10.1016/j.egypro.2015.12.322.
[25] T. Ono, H. Nagano, S. Shiratori, K. Shimano, S. Kato, Analysis of defogging performance, thermal comfort, and energy saving for HVAC system optimization in passenger vehicles, E3S Web Conf. 111 (2019) 01033, https://doi.org/10.1051/e3sconf/201911101033.
[26] B.S. Abdulnour, Numerical simulation of vehicle defroster flow field, SAE Technical Paper Series, 1998. http://doi.org/10.4271/980285.
[27] K.J. Nasr, B.S. Abdulnour, G.C. Wiklund, State of Knowledge and Current Challenges in Defrosting Automotive Windshields, SAE Technical Paper Series, 1998. http://doi.org/10.4271/980293.
[28] A. Aroussi, A. Hassan, B. Clayton, B.S. AbdulNour, E. Rice, Improving Vehicle Windshield Defrosting and Demisting, SAE Technical Paper Series, 2000. http://doi.org/10.4271/2000-01-1278.
[29] A. Aroussi, S.A. Ghani, A. Hassan, B.S. Abdulnour, Assessing the Performance of Electrically Heated Windshield, SAE Technical Paper Series, 2002. http://doi.org/10.4271/2002-01-0225.
[30] A. Aroussi, A. Hassan, B.R. Clayton, B.S. Abdulnour, An Assessment of Vehicle Side-Window Defrosting and Demisting Process, SAE Technical Paper Series, 2001. http://doi.org/10.4271/2001-01-0289.
[31] R.A. Dwiartono, C.W. Somerton, B. Abdulnour, P. Hoke, The Use of Numerical Simulations to Perform Engineering Calculations of Window Defogging, SAE Technical Paper Series, 2005. http://doi.org/10.4271/2005-01-2054.
[32] R.B. Kharat, M.R. Nandgaonkar, S.R. Kajale, V.V. Ranade, S.K. Mahajan, Modeling of In-Cabin Climate and Fogging of Windshield, SAE Technical Paper, Series, 2007. http://doi.org/10.4271/2007-01-0767.
[33] ANSYS Fluent 17.0 User's Guide, ANSYS, Inc, 2015.
[34] D. Zeng, Y. Ao, X. Zhang, Z. Liu, Engineering Thermodynamics, third ed., Higher Education Press, Beijing, China, 2002.
[35] W. Ambrosini, M. Bucci, N. Forgione, et al., Comparison and analysis of the condensation benchmark results, 3rd European Review Meeting on Severe Accident Research, (2008).
[36] L. Vyskocil, J. Schmid, J. Macek, CFD simulation of air–steam flow with condensation, Nucl. Eng. Des. 279 (2014) 147–157, https://doi.org/10.1016/j.nucengdes.2014.02.014.
[37] Y. Yang, J. Cheng, Y. Huang, Analysis on the influence of gap flow around a tractor-trailer, 13th International Conference on Heat Transfer, Fluid Mechanics and Thermodynamics, (2017).